

# Filters, Reproducing Kernel, and Adaptive Meshfree Method

Yang You<sup>1</sup>, Jiun-Shyan Chen<sup>2</sup>, and Hongsheng Lu<sup>3</sup>

*Department of Civil & Environmental Engineering  
University of California, Los Angeles  
5731G Boelter Hall  
Los Angeles, CA 90095-1593*

*Submitted to Computational Mechanics, July, 2002*

*Revised, February, 2003*

---

<sup>1</sup> Former Graduate student.

<sup>2</sup> Corresponding author. Professor, Department of Civil & Environmental Engineering, UCLA, 5731 G Boelter hall, Los Angeles, CA 90095-1593. E-mail: jschen@seas.ucla.edu

<sup>3</sup> Postdoctoral Associate.

## **Abstract**

Reproducing kernel, with its intrinsic feature of moving averaging, can be utilized as a low-pass filter with scale decomposition capability. The discrete convolution of two  $n^{\text{th}}$  order reproducing kernels with arbitrary support size in each kernel results in a filtered reproducing kernel function that has the same reproducing order. This property is utilized to separate the numerical solution into an unfiltered lower order portion and a filtered higher order portion. As such, the corresponding high-pass filter of this reproducing kernel filter can be used to identify the locations of high gradient, and consequently serves as an operator for error indication in meshfree analysis. In conjunction with the naturally conforming property of the reproducing kernel approximation, a meshfree adaptivity method is also proposed.

**Key Words:** filter kernel, error indicator, adaptive analysis, reproducing kernel, meshfree

## 1. Introduction

Filters are useful tools in signal processing, separating a given signal  $f(t)$  into different frequency bands. Its application ranges from noise and echo reduction, to audio/video compression and synthesis, and to medical imaging (Blinchikoff and Zverev, 1976, Sheno, 1995, Kalouptsidis, 1996, Smith, 1997). These applications utilize a filter's ability to decompose the low and high frequency components of a signal. Filters can be generally classified as low-pass filter and high-pass filter according to their pass-band and stop-band characteristics. A low-pass filter is designed to block all frequencies above the cut-off frequency (the stop-band), while passing all frequencies below the cut-off frequency (pass-band). In contrast, a high-pass filter passes all high frequencies while substantially filtering smooth data.

An important family of filters, frequently employed in recent years, is the family of wavelet functions (Chui, 1992, Daubechies, 1992, Strang, 1996). In multi-resolution studies, the scaling function is applied as a low-pass filter to various scales, with increasing resolution (increasing range of pass-band) as the scale increases. The wavelet functions form a sequence of filters that yield a band-pass decomposition of high frequencies. The advantage of wavelet filters is that a given signal can be decomposed into a sequence of consecutive frequency bands corresponding to the intrinsic scales of the wavelet functions (Chui, 1992, Strang, 1996). The analogy between the signal in time domain and the response in spatial domain can be easily demonstrated. Liu et al. (1995a) first proposed the concept of multiple-scale Reproducing Kernel Particle Method (RKPM) based on the wavelet theory. Liu et al. (1995b, 1996, 1997a, 1997b) and Li et al. (1996, 1999) conducted several studies with respect to multi-resolution analysis using reproducing kernels for edge detection and aliasing control.

A study of the relationship between the filter kernel and the reproducing kernel is conducted in this paper. The order of reproducing condition and the support size are the two control parameters in the construction of reproducing kernel as a low-pass filter. It is shown that the discrete convolution of two  $n^{\text{th}}$  order reproducing kernels with arbitrary support size in each kernel results in a filtered reproducing kernel function that has the same reproducing order. This property, in conjunction with the intrinsic scale feature of the reproducing kernel function,

provides a unique capability to locate the regions of high gradient in the meshfree analysis. The output of the high-pass filter is proposed as the error indicator for adaptive meshfree analysis.

The layout of the paper is as follows. The basic concept of filters and the filter kernels are explained in Section 2. Section 3 reviews the Reproducing Kernel approximation in continuous and discrete forms. A study on the reproducing kernel as low-pass filter kernel is conducted in Section 4, together with the formulation of a two-scale decomposition of a displacement field. Based on the discussion in Section 4, an error indicator is proposed in Section 5, and an adaptive meshfree formulation is also introduced. Numerical experiments are shown in Section 6 to illustrate the performance of the error indicator and the adaptive meshfree method. Concluding remarks are given in Section 7.

## 2. Low and High-pass Filters

Filters provide two basic functions: separation of signals that have been combined (de-noising) and restoration of signals that have been distorted in some way. Each filter has a pass-band (the unaltered frequency range after filtering), a stop-band (the excluded frequency range), and a transition-band (the frequency range in between). For a filter with fast roll-off property, the transition-band is narrow enough to be ignored.

One simple example of a low-pass filter and a high-pass filter is given herein in discrete domain. Signals are expressed as  $x[t_n]$ , where  $\{t_n\}_{n=-\infty}^{\infty}$  is the set of discrete time used for representing the data. The simplest low-pass filter is defined by its operation on the input signal as:

$$y[t_n] = \frac{x[t_n] + x[t_{n-1}]}{2}, \quad (2.1)$$

and the high-pass filter is in a similar way:

$$z[t_n] = \frac{x[t_n] - x[t_{n-1}]}{2}. \quad (2.2)$$

The above low-pass filter is actually a *moving average* operation involving the point  $x[t_n]$  and its previous point  $x[t_{n-1}]$  with an equal weight  $\frac{1}{2}$ . The high-pass filter is a *moving difference* operation involving the same set of information.

A filter is classified by its impulse response  $f(t)$ , also called the filter kernel, which is the output signal produced given by unit impulse as the input. The output signal  $y(t)$  of a general input signal  $x(t)$  can be obtained through the convolution of  $x(t)$  and the filter kernel  $f(t)$ :

$$y(t) = x(t) * f(t) = \int_{-\infty}^{\infty} x(\tau) f(t - \tau) d\tau, \quad (2.3)$$

or in the discrete form

$$y[t_n] = x[t] \hat{*} f[t] = \sum_{k=-\infty}^{\infty} x[t_k] f[t_{n-k}]. \quad (2.4)$$

For this filtering transformation to be valid, the input signal  $x(t)$  and the output signal  $y(t)$  should belong to the same function space, e.g., the  $L_p$  space. A well-posedness statement provides a requirement for the kernel function  $f(t)$ :

*For each input signal  $x(t)$  in  $L_p$ , the output signal  $y(t) = x(t) * f(t)$  is well defined and belongs to  $L_p$  if the filter kernel function  $f(t)$  is absolutely integrable, that is:*

$$\int |f(t)| dt < \infty \text{ or } f(t) \in L_1. \quad (2.5)$$

The discrete well-posedness statement is:

*For each input signal  $x[t_n]$  in  $l_p$ , the output signal  $y[t_n] = x[t] \hat{*} f[t]$  is well defined and belongs to  $l_p$  if the filter kernel function  $f[t_n]$  is absolutely summable, i.e.*

$$\sum |f(t_n)| < \infty \text{ or } f[t_n] \in l_1. \quad (2.6)$$

The spectral responses of both the input and output signals can be analyzed using Fourier analysis. The convolution formula of Fourier transform implies

$$F_y(\omega) = F_x(\omega) F_f(\omega), \quad (2.7)$$

where  $F_f(\omega) = \int_{-\infty}^{\infty} f(t) e^{-i\omega t} dt$  is the spectral response of  $f(t)$ . For a low-pass filter kernel  $f(t)$ , its spectral response ranges from 0 to  $\omega_c$ . This range is the pass-band of  $f(t)$ .

Hence the spectral response  $F_y(\omega)$  of the output  $y(t)$  will also be inside this pass-band, i.e., the frequency component of the input  $x(t)$  outside the pass-band is removed. An analogous argument can be made for high-pass filter kernels.

An important family of filters is the family of wavelet functions (Chui, 1992, Daubechies, 1992, Strang et al., 1996). In wavelet multi-resolution construction, the scaling functions  $\varphi_{m,k}(x) = 2^{m/2}\varphi(2^m x - k)$  are used as a low-pass filter on various scales, with increasing resolution (increasing range of the pass-band) as the scale  $m$  increases. The wavelet functions  $\psi_{m,k}(x) = 2^{m/2}\psi(2^m x - k)$  form a sequence of filters that yield a band-pass decomposition of high frequencies. With wavelet filters, a given signal can be decomposed into a sequence of consecutive frequency bands corresponding to the intrinsic scales of the wavelet functions. Figure 2.1 illustrates some common low-pass filter kernels and their spectral responses .

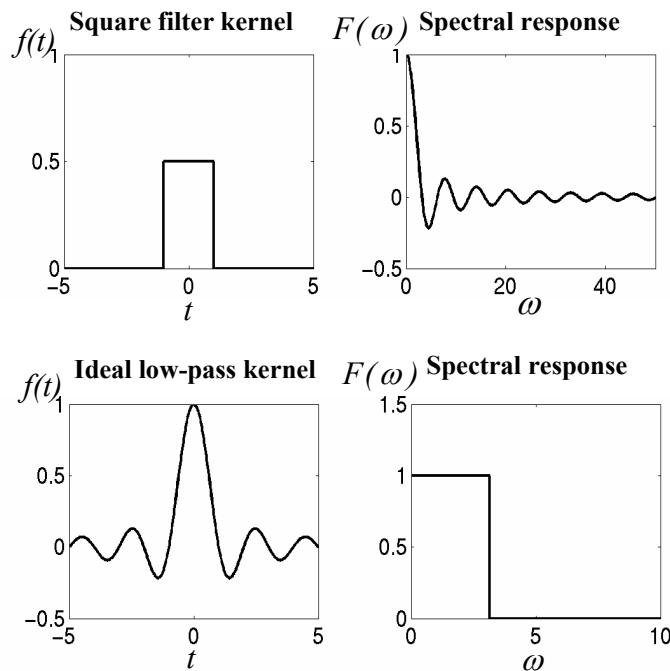


Figure 2.1 Low-pass filters and their spectral responses

### 3. Reproducing Kernels

Reproducing kernel can be used as a filter kernel with special properties. For a given function  $u(x)$  in a domain  $\Omega$ , the convolution of  $u(x)$  and the reproducing kernel  $\Phi^a(x)$  is

$$u^R(x) = u(x) * \Phi_n^a(x) = \int_{\Omega} u(\tilde{x}) \Phi_n^a(x; x - \tilde{x}) d\tilde{x}, \quad (3.1)$$

where the function  $\Phi_n^a$  is the  $n^{\text{th}}$  order reproducing kernel which meets  $n^{\text{th}}$  order reproducing conditions, and “ $a$ ” denotes the kernel support size. Substituting Taylor series expansion of a function  $u(\tilde{x})$  at point  $x$  into Eq. (3.1) leads to

$$\begin{aligned} u^R(x) = & u(x)m_0(x) + u^{(1)}(x)m_1(x) + \frac{1}{2!}u^{(2)}(x)m_2(x) \\ & + \dots + \frac{1}{n!}u^{(n)}(x)m_n(x) + \frac{1}{(n+1)!}u^{(n+1)}(\xi)m_{n+1}(x) \end{aligned} \quad (3.2)$$

where  $m_k(x) = \int_{\Omega} (x - \tilde{x})^k \Phi_n^a(x; x - \tilde{x}) d\tilde{x}$ , and  $u^{(k)} = d^k u / dx^k$ . Reproduction of a polynomial up to degree  $n$  requires

$$m_k(x) = \delta_{k0}, \quad k = 0, 1, 2, \dots, n. \quad (3.3)$$

To meet the  $n$ -th order reproducing conditions in Eq. (3.3), the reproducing kernel  $\Phi_n^a$  is expressed as (Liu et al., 1995c)

$$\Phi_n^a(x; x - \tilde{x}) = \mathbf{P}^T(x - \tilde{x}) \mathbf{b}(x) \phi^a(x - \tilde{x}) \quad (3.4)$$

$$\mathbf{P}^T(x) = [1, x, \dots, x^n], \quad \mathbf{b}(x) = [b_0(x), b_1(x), \dots, b_n(x)]^T, \quad (3.5)$$

and  $\phi^a$  is a kernel function, for instance, a B-spline function or a truncated Gauss function, with compact support  $a$ . The coefficient  $\mathbf{b}(x)$  can be obtained by solving the equation of reproducing conditions in Eq. (3.3) to yield

$$\mathbf{b}(x) = \mathbf{M}^{-1}(x)\mathbf{P}(0) \quad (3.6)$$

$$\mathbf{M}(x) = \int_{\Omega} \mathbf{P}(x - \tilde{x})\mathbf{P}^T(x - \tilde{x})\phi^a(x - \tilde{x})d\tilde{x} . \quad (3.7)$$

The reproducing kernel convolution of Eq. (3.1) is thus rewritten as

$$u^R(x) = \mathbf{P}^T(0) \int_{\Omega} \mathbf{M}^{-1}(x)\mathbf{P}(x - \tilde{x})\phi^a(x - \tilde{x})u(\tilde{x})d\tilde{x} . \quad (3.8)$$

The discrete reproduction of a function  $u(x)$ , denoted by  $u^h(x)$ , with a reproducing kernel is defined as

$$u^h(x) = \sum_{l=1}^{NP} \Phi_n^a(x; x - x_l)u_l , \quad (3.9)$$

where  $NP$  is the number of discrete points, the superscript  $n$  refers to the reproducing order in this approximation, and  $\Phi_n^a(x; x - x_l)$  is the discrete reproducing kernel that is formed similar to the continuous case:

$$\Phi_n^a(x; x - x_l) = \mathbf{P}^T(x - x_l)\mathbf{b}(x)\phi^a(x - x_l) . \quad (3.10)$$

By enforcing the discrete  $n^{\text{th}}$  order reproducing conditions:

$$x^k \hat{*} \Phi_n^a(x) = \sum_{l=1}^{NP} \Phi_n^a(x; x - x_l)x_l^k = x^k , \quad k = 0, 1, \dots, n , \quad (3.11)$$

the coefficient vector  $\mathbf{b}(x)$  is obtained:

$$\mathbf{b}(x) = \mathbf{M}^{-1}(x)\mathbf{P}(0) \quad (3.12)$$

$$\mathbf{M}(x) = \sum_{I=1}^{NP} \mathbf{P}(x-x_I)\mathbf{P}^T(x-x_I)\phi^a(x-x_I). \quad (3.13)$$

Finally, the discrete reproducing kernel approximation yields

$$u^h(x) = \sum_{I=1}^{NP} \mathbf{P}^T(0)\mathbf{M}^{-1}(x)\mathbf{P}(x-x_I)\phi^a(x-x_I)u_I = \sum_{I=1}^{NP} \Phi_n^a(x; x-x_I)u_I. \quad (3.14)$$

The extension to multi-dimension is straightforward: simply by including complete multi-dimensional monomial bases in the  $\mathbf{P}$  vector and employing the multi-dimensional kernel function  $\phi^a(\mathbf{x}-\mathbf{x}_I)$ . The multi-dimensional  $n^{\text{th}}$  order reproducing kernel meets the following reproducing conditions:

$$x_1^i x_2^j x_3^k \hat{*} \Phi_n^a(\mathbf{x}) = x_1^i x_2^j x_3^k, \quad i+j+k = 0, 1, \dots, n. \quad (3.15)$$

The meshfree solution of the partial differential equation is obtained by employing the Galerkin approximation in conjunction with the reproducing kernel approximation in Eq. (3.14), see Liu et al. (1995a-c, 1996) and Chen et al. (1996, 2000, 2001).

## 4. Reproducing Kernel as a Low-Pass Filter

### 4.1 Reproducing kernel filter

The build-in features of the  $n^{\text{th}}$  order reproducing kernel can be utilized to form a special low-pass filter with the properties in which the polynomials of degree less than  $n+1$  are completely retained. Since the reproducing kernels are continuous with compact support, it is easy to see that  $\Phi_n^a(x) \in L_1$ . Hence the well-posedness condition is satisfied in the reproducing kernels.

The order of reproducing condition and the support size are the two control parameters in the construction of reproducing kernels. Figure 4.1 illustrates the spectral responses of reproducing kernels with different reproducing orders while keeping the same support size. It is observed that the pass-band expands as the reproducing order of the kernel function increases. Thus, the reproducing kernel functions provide higher resolution as the reproducing order increases. The sequence  $\{\Phi_1^a(x), \Phi_2^a(x), \dots, \Phi_n^a(x), \dots\}$ , in which  $n$  denotes the reproducing order, forms a family of low-pass filters with an expanding pass-band.

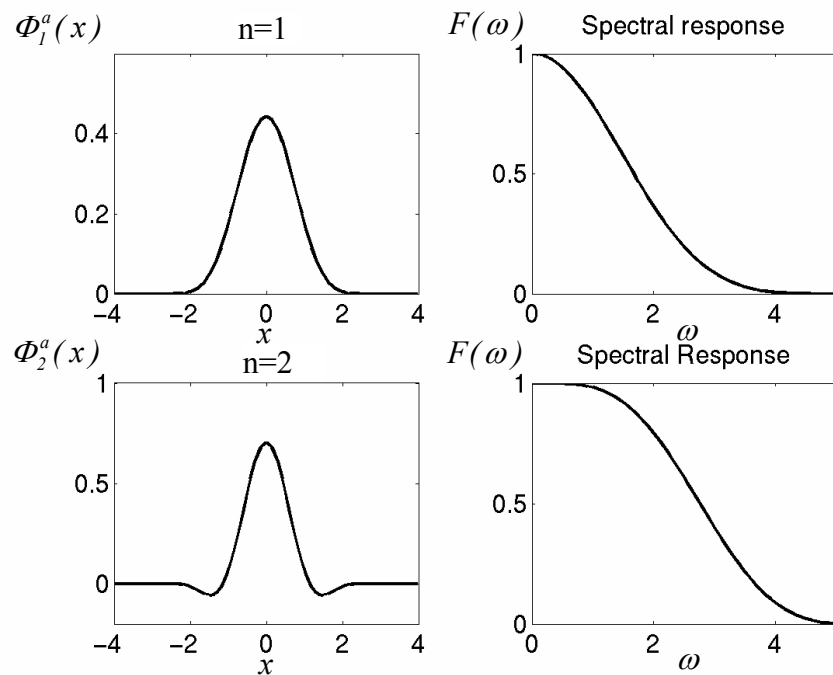


Figure 4.1 Reproducing kernels and their spectral response

Next, the spectral responses of the reproducing kernels  $\Phi_l^a, \Phi_l^{2a}, \Phi_l^{3a}, \Phi_l^{4a}$  with  $a=1.1$  are presented in Fig. 4.2. It is shown that the pass-bands diminish as the support size increases. The functions  $\{\Phi_m^a(x), \Phi_m^{2a}(x), \dots, \Phi_m^{2^n a}(x), \dots\}$  form a sequence of low-pass filters with shrinking pass-bands. In Figure 4.3, the 1<sup>st</sup> order reproducing kernels with different support sizes are used to approximate a step function. The reproducing kernel with smaller support size better captures a step function due to its wider frequency band.

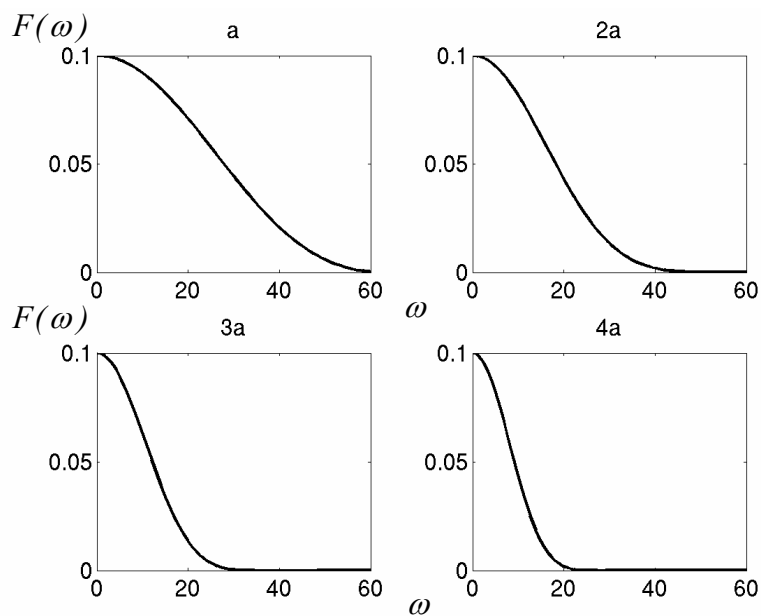


Figure 4.2 Spectral response of  $\Phi_l^a, \Phi_l^{2a}, \Phi_l^{3a}, \Phi_l^{4a}$

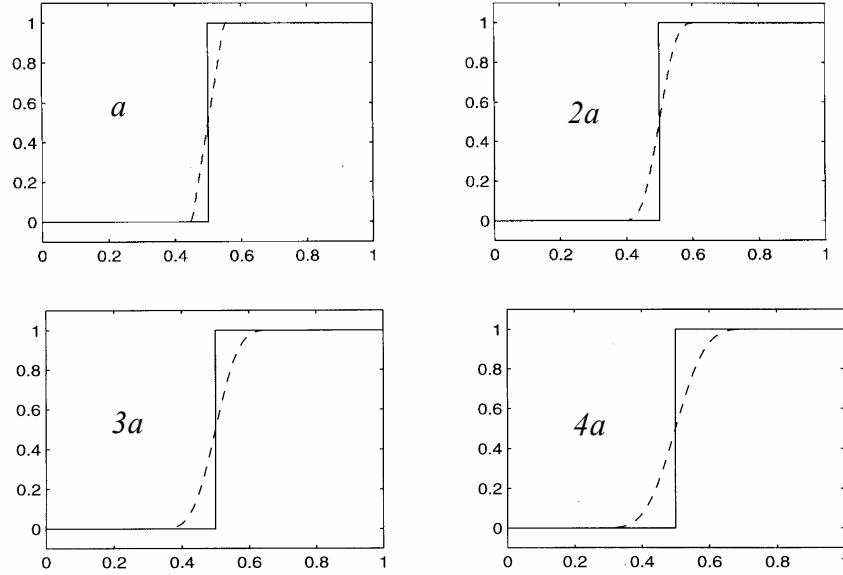


Figure 4.3 RK approximation of a step function with  $\Phi_l^a, \Phi_l^{2a}, \Phi_l^{3a}, \Phi_l^{4a}$

To this end, we define reproducing kernel as a low-pass filter,

$$l(x) = \Phi_n^a(x) . \quad (4.1)$$

A corresponding high-pass filter is defined as

$$h(x) = \delta(x) - l(x), \quad (4.2)$$

where  $\delta(x)$  is the Dirac delta function. Note that the spectral response of  $\delta(x)$  covers all frequency,

$$F(\omega) = \int_{-\infty}^{\infty} \delta(x) e^{-i\omega x} dx = 1 . \quad (4.3)$$

The spectral response of the high-pass filter kernel  $h(x)$  is exactly the complement of that of the low-pass filter kernel  $l(x)$ , as shown in Figure 4.4.

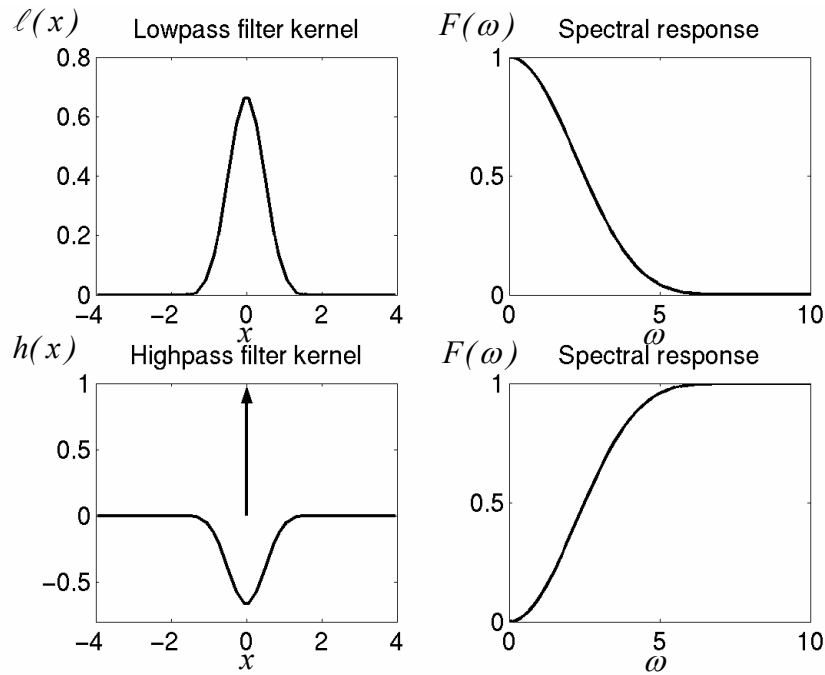


Figure 4.4 Low-pass and high-pass filter kernels and their spectral response

Together, the two filters form a two-scale decomposition of the given function:

$$u(x) = u(x) * l(x) + u(x) * h(x) = u(x) * l(x) + u(x) * (\delta(x) - l(x)). \quad (4.4)$$

An example is used to illustrate the reproducing kernel two-scale decomposition. Given a function  $u(x) = x^2$  in  $[0, 1]$  that has been blurred by a noise  $0.1 \sin(20\pi x)$ , as shown in Fig. 4.5. A 2<sup>nd</sup>-order reproducing kernel completely filters out the noise. Conversely, the noise can be isolated using the corresponding high-pass filter. This property does not always exist in other filter kernels, such as B-spline shown in Fig 4.6, where errors exist near the boundaries.

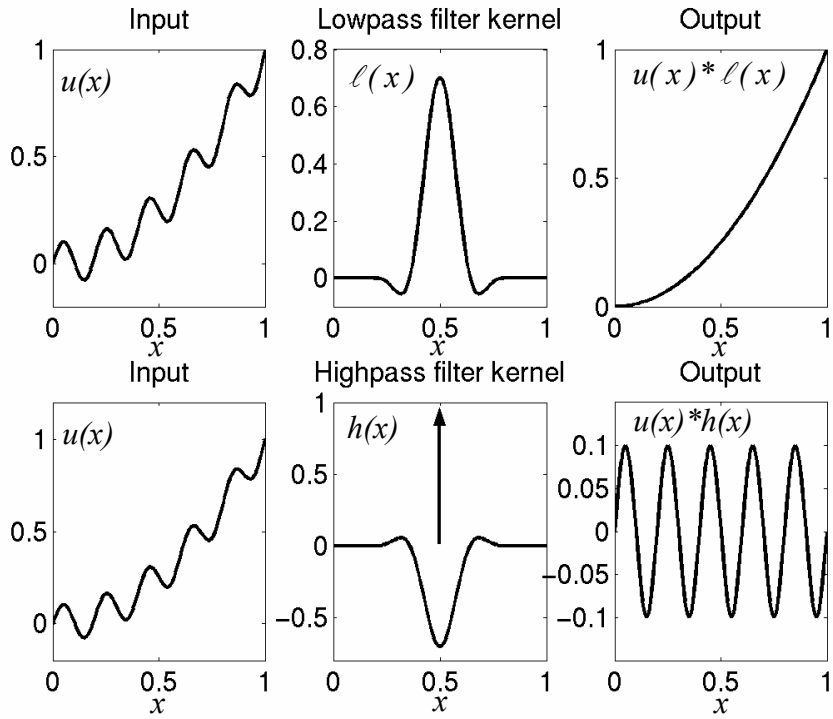


Figure 4.5 Filtering of  $x^2 + 0.1 \sin(20\pi x)$

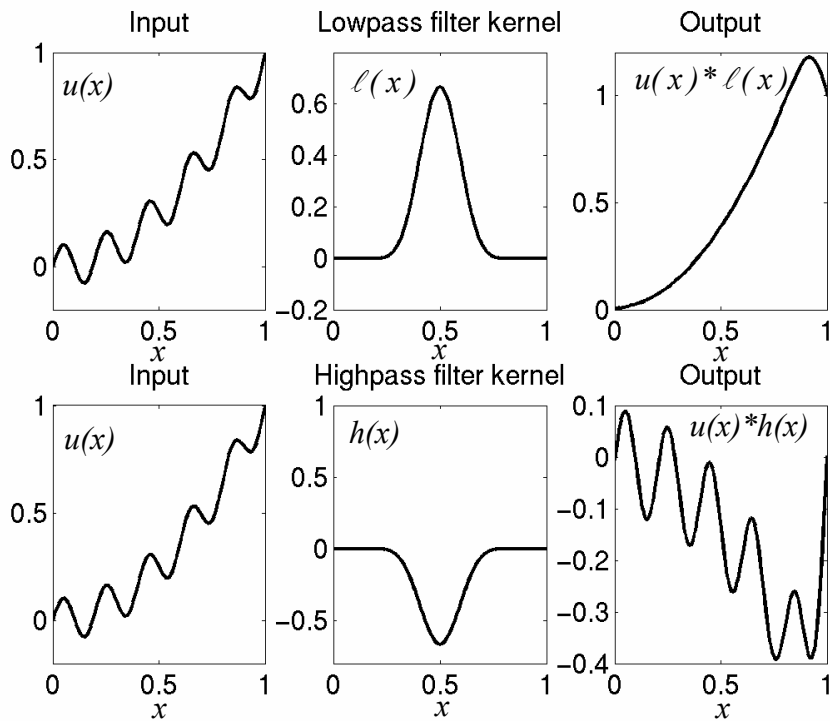


Figure 4.6 Filtering through a Cubic B-Spline kernel

## 4.2 Error indicator

The reproducing kernels have been used as the approximation functions in obtaining the meshfree solution of partial differential equations. Let  $u^a(\mathbf{x})$  be the meshfree solution of a partial differential equation obtained using reproducing kernel  $\{\Phi_n^a(\mathbf{x} - \mathbf{x}_l)\}_{l=1}^{NP}$  of scale- $a$  as the shape functions in the discretization of the Galerkin approximation. We write  $u^a(x)$  as

$$u^a(\mathbf{x}) = \sum_{l=1}^{NP} \Phi_n^a(\mathbf{x} - \mathbf{x}_l) u_l^a, \quad (4.5)$$

where  $u_l^a$  is the coefficients of approximation obtained from meshfree solution of a partial differential equation. For convenience, we use  $\Phi_n^a(\mathbf{x} - \mathbf{x}_l) \equiv \Phi_n^a(\mathbf{x}; \mathbf{x} - \mathbf{x}_l)$  to denote the discrete counterpart of  $\Phi_n^a(\mathbf{x})$ . The scale- $2a$  reproducing kernel filtering of  $u^a(x)$  is

$$\begin{aligned} \tilde{u}^{2a}(\mathbf{x}) &= u^a(\mathbf{x}) \hat{*} \Phi_n^{2a}(\mathbf{x}) \\ &= \sum_{l=1}^{NP} \tilde{\Phi}_n^{2a}(\mathbf{x} - \mathbf{x}_l) u_l^a \end{aligned} \quad (4.6)$$

where

$$\begin{aligned} \tilde{\Phi}_n^{2a}(\mathbf{x} - \mathbf{x}_l) &= \Phi_n^a(\mathbf{x} - \mathbf{x}_l) \hat{*} \Phi_n^{2a}(\mathbf{x}) \\ &= \sum_{j=1}^{NP} \Phi_n^a(\mathbf{x}_j - \mathbf{x}_l) \Phi_n^{2a}(\mathbf{x} - \mathbf{x}_j) \end{aligned} \quad (4.7)$$

We call  $\tilde{\Phi}_n^{2a}(\mathbf{x})$  the filtered reproducing kernel function. The reproducing conditions of  $\Phi_n^a(\mathbf{x})$  and  $\Phi_n^{2a}(\mathbf{x})$  give

$$\sum_{l=1}^{NP} \Phi_n^a(\mathbf{x} - \mathbf{x}_l) x_{1l}^i x_{2l}^j x_{3l}^k = x_1^i x_2^j x_3^k, \quad \sum_{l=1}^{NP} \Phi_n^{2a}(\mathbf{x} - \mathbf{x}_l) x_{1l}^i x_{2l}^j x_{3l}^k = x_1^i x_2^j x_3^k \quad \text{for } 0 \leq i + j + k \leq n. \quad (4.8)$$

It can be shown that the filtered reproducing kernel function  $\tilde{\Phi}_n^{2a}(\mathbf{x})$  also satisfies the  $n^{\text{th}}$  order reproducing condition as follows:

$$\begin{aligned}
& \sum_{l=1}^{NP} \tilde{\Phi}_n^{2a}(\mathbf{x} - \mathbf{x}_l) x_{1l}^i x_{2l}^j x_{3l}^k \\
&= \sum_{l=1}^{NP} \left( \sum_{j=1}^{NP} \Phi_n^a(\mathbf{x}_j - \mathbf{x}_l) \Phi_n^{2a}(\mathbf{x} - \mathbf{x}_j) \right) x_{1l}^i x_{2l}^j x_{3l}^k \\
&= \sum_{j=1}^{NP} \left( \sum_{l=1}^{NP} \Phi_n^a(\mathbf{x}_j - \mathbf{x}_l) x_{1l}^i x_{2l}^j x_{3l}^k \right) \Phi_n^{2a}(\mathbf{x} - \mathbf{x}_j) \\
&= \sum_{j=1}^{NP} x_{1j}^i x_{2j}^j x_{3j}^k \Phi_n^{2a}(\mathbf{x} - \mathbf{x}_j) \\
&= x_1^i x_2^j x_3^k
\end{aligned} \tag{4.9}$$

The above property shows that the discrete convolution of two  $n^{\text{th}}$  order reproducing kernels generates another  $n^{\text{th}}$  order reproducing kernel. Following similar procedures, it also can be shown that the reproducing order of  $\Phi_m^a(\mathbf{x} - \mathbf{x}_l) \hat{*} \Phi_n^{2a}(\mathbf{x})$  is  $\min(m, n)$ .

The meshfree solution  $u^a(\mathbf{x})$  can be decomposed into the output of low-pass and high-pass filters as

$$\begin{aligned}
u^a(\mathbf{x}) &= u^a(\mathbf{x}) \hat{*} \Phi_n^{2a}(\mathbf{x}) + u^a(\mathbf{x}) \hat{*} [\delta(\mathbf{x}) - \Phi_n^{2a}(\mathbf{x})] \\
&= \sum_{l=1}^{NP} \tilde{\Phi}_n^{2a}(\mathbf{x} - \mathbf{x}_l) u_l^a + \sum_{l=1}^{NP} [\Phi_n^a(\mathbf{x} - \mathbf{x}_l) - \tilde{\Phi}_n^{2a}(\mathbf{x} - \mathbf{x}_l)] u_l^a \\
&= \tilde{u}^{2a}(\mathbf{x}) + \tilde{w}^{2a}(\mathbf{x})
\end{aligned} \tag{4.10}$$

where  $\tilde{u}^{2a}(\mathbf{x})$  is the output of  $u^a(\mathbf{x})$  after it has been filtered through the low-pass filter  $\Phi_n^{2a}(\mathbf{x})$  of scale- $2a$ . The term  $\tilde{w}^{2a}(\mathbf{x})$  is the output of  $u^a(\mathbf{x})$  through the high-pass filter

kernel  $\delta(\mathbf{x}) - \Phi_n^{2a}(\mathbf{x})$ , and can be used as the high gradient indicator for adaptive analysis described in the next section. Note that the above decomposition degenerates to Liu et al. (1995b, 1996) if  $\tilde{\Phi}_n^{2a}$  is replaced by  $\Phi_n^{2a}$ .

To illustrate,  $u^a(\mathbf{x})$  is expressed in the following form:

$$u^a(\mathbf{x}) = u_L^a(\mathbf{x}) + u_H^a(\mathbf{x}), \quad (4.11)$$

where  $u_L^a(\mathbf{x})$  is the lower order component of  $u^a(\mathbf{x})$  by Taylor expansion up to  $n^{\text{th}}$  order, and  $u_H^a(\mathbf{x})$  is the remainder that contains the higher order component of  $u^a(\mathbf{x})$ . By substituting Eq. (4.11) into Eq. (4.6) and using the reproducing properties of  $\Phi_n^{2a}$ , it can be shown that the reproducing kernel filtering only alters the higher order component of  $u^a(\mathbf{x})$ , i.e.,

$$\tilde{u}^{2a}(\mathbf{x}) = u_L^a(\mathbf{x}) + \tilde{u}_H^a(\mathbf{x}), \quad (4.12)$$

where

$$\tilde{u}_H^a(\mathbf{x}) = u_H^a(\mathbf{x}) \hat{*} \Phi_n^{2a}(\mathbf{x}). \quad (4.13)$$

Thus, the output of the high-pass filter  $\tilde{w}^{2a}(\mathbf{x})$  in Eq. (4.10) serves as an indicator of the higher order component of  $u^a(\mathbf{x})$ :

$$\tilde{w}^{2a}(\mathbf{x}) = u^a(\mathbf{x}) - \tilde{u}^{2a}(\mathbf{x}) = u_L^a(\mathbf{x}) - u_H^a(\mathbf{x}) \hat{*} \Phi_n^{2a}(\mathbf{x}). \quad (4.14)$$

## 5. Adaptive Meshfree Method

Adaptive method is an effective approach to achieve accuracy and efficiency simultaneously. The naturally conforming property of meshfree approximation offers considerable advantages in adaptive analysis. It allows arbitrary insertion and deletion of particles without the burden of compatibility requirement.

### 5.1 Error indicator in energy norm

As discussed in the previous section, the pass-band of reproducing kernel approximation can be adjusted by choosing the different reproducing order and support size. The sequence  $\{\Phi_1^a(\mathbf{x}), \Phi_2^a(\mathbf{x}), \dots, \Phi_n^a(\mathbf{x}), \dots\}$  forms a family of low-pass filters with an expanding pass-band, and the sequence  $\{\Phi_n^a(\mathbf{x}), \Phi_n^{2a}(\mathbf{x}), \dots, \Phi_n^{2^m a}(\mathbf{x}), \dots\}$  forms a set of low-pass filters with shrinking pass-band. It is also shown in Section 4 that the location of high gradient in the numerical solution  $u^a(\mathbf{x})$  can be identified by examining the output of  $u^a(\mathbf{x})$  passing through the high-pass filter of reproducing kernel. Similar procedures can be applied to stress. The output of stress  $\sigma^*(\mathbf{x})$  after filtering through the low-pass filter  $\Phi_n^a(\mathbf{x})$  reads

$$\tilde{\sigma}^{2a}(\mathbf{x}) = \sigma^a(\mathbf{x}) \hat{*} \Phi_n^{2a}(\mathbf{x}). \quad (5.1)$$

The error indication of  $e_\sigma = \sigma - \sigma^a$ , denoted as  $e_\sigma^*$ , is obtained from the high-pass filter:

$$e_\sigma^*(\mathbf{x}) = \sigma^a(\mathbf{x}) \hat{*} [\delta(\mathbf{x}) - \Phi_n^{2a}(\mathbf{x})] = \sigma^a(\mathbf{x}) - \tilde{\sigma}^{2a}(\mathbf{x}). \quad (5.2)$$

The relative error in energy norm  $\eta^*$  and the nodal energy error density  $\rho_l^*$  are defined as

$$\eta^* = \|e_\sigma^*\|_E / \|\sigma^a\|_E \quad (5.3)$$

$$\|e_\sigma^*\|_E = \left\{ \frac{1}{2} \sum_{l=1}^l e_\sigma^*(\mathbf{x}_l)^T \mathbf{C}^{-1} e_\sigma^*(\mathbf{x}_l) A_l \right\}^{1/2} \quad (5.4)$$

$$\|\boldsymbol{\sigma}^a\|_E = \left\{ \frac{1}{2} \sum_{l=1}^L \boldsymbol{\sigma}^{aT}(\mathbf{x}_l) \mathbf{C}^{-1} \boldsymbol{\sigma}^a(\mathbf{x}_l) A_l \right\}^{1/2} \quad (5.5)$$

$$\rho_l^* = \left( \frac{1}{2} \mathbf{e}_\sigma^*(\mathbf{x}_l)^T \mathbf{C}^{-1} \mathbf{e}_\sigma^*(\mathbf{x}_l) \right)^{1/2} \quad (5.6)$$

where  $A_l$  is the nodal area obtained from the Voronoi diagram.

## 5.2 Adaptive refinement

Adaptive procedures have been proposed in meshfree analysis, for example, Lu and Chen (2002) and Liu and Tu (2002). The adaptive procedures using Voronoi cell as a reference for node insertion introduced by Lu and Chen (2002) is employed in this work.

Given a set  $S$  of NP distinct particles in  $R^d$ , a Voronoi diagram is the partition of  $R^d$  into NP polyhedral regions  $V(P_l)$ ,  $P_l \in S$ . Each region  $V(P_l)$ , called the Voronoi cell of  $P_l$ , is defined as the set of points in  $R^d$  which are closer to  $P_l$  than to any other points in  $S$ , i.e.

$$V(P_l) = \{ \mathbf{x} \in R^d \mid \text{dist}(\mathbf{x}, P_l) \leq \text{dist}(\mathbf{x}, Q_l) \quad \forall Q_l \in S - P_l \}. \quad (5.7)$$

The topology of Voronoi diagram is used as a reference for inserting particles. Using the properties of Voronoi cell boundary which is the perpendicular bisector hyper-plane of a line connecting any two particles, new particles are added at the vertices of the Voronoi cell as shown in Fig. 5.1. Multi-level adaptive refinements for initially uniform and non-uniform particles are shown in Figures 5.2 and 5.3.

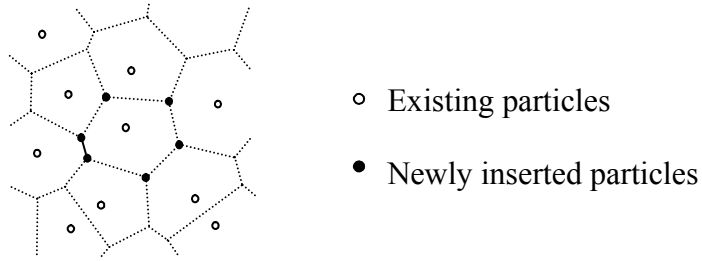


Figure 5.1 Insertion of particles based on a Voronoi diagram

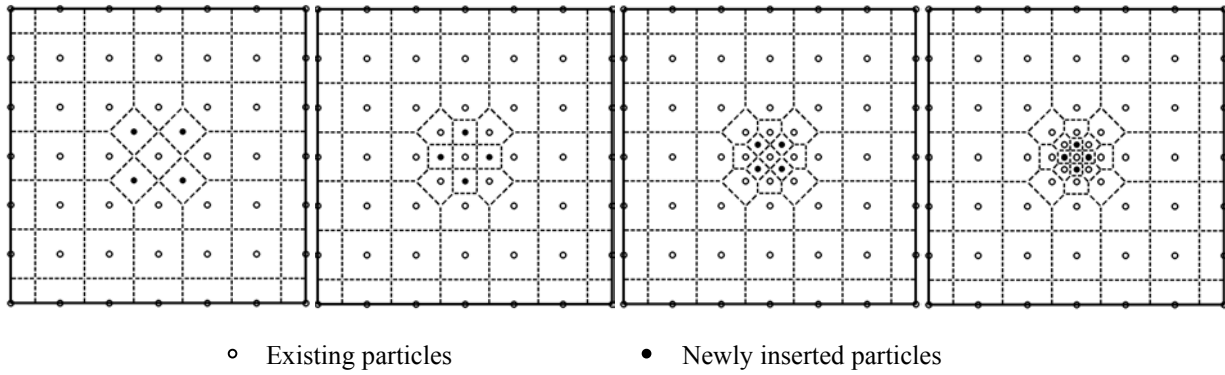


Figure 5.2 Multi-level adaptive refinements on a set of uniformly distributed particles

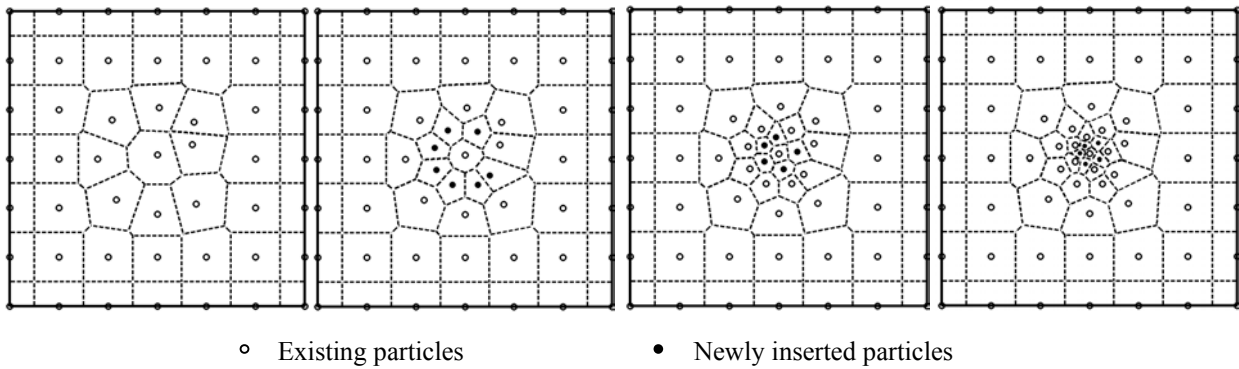


Figure 5.3 Multi-level adaptive refinements on a set of non-uniformly distributed particles

### 5.3 Shape function update

In response to the newly added or deleted particles, the  $\mathbf{M}(\mathbf{x})$  matrix in the reproducing kernel (Eq. (3.13)) of the existing particles must be reconstructed locally to maintain the reproducing order in the reproducing kernel approximation as follows:

$$\mathbf{M}(\mathbf{x}) = \mathbf{M}_{old}(\mathbf{x}) \pm \sum_{I=1}^{NP_{new}} \mathbf{P}(\mathbf{x} - \mathbf{x}_I) \mathbf{P}^T(\mathbf{x} - \mathbf{x}_I) \phi^a(\mathbf{x} - \mathbf{x}_I). \quad (5.8)$$

Note that at  $\mathbf{x}$ , the moment matrix  $\mathbf{M}(\mathbf{x})$  changes only when  $\mathbf{x}$  is in a region covered by the kernels  $\phi^a$  associated with the adaptive particles. In Fig. 5.4, inserting a particle between particles 6 and 7 requires reconstruction of the reproducing kernels of particles 4, 5, 6, 7, 8, 9 and the new reproducing kernel of the new particle 12. Figure 5.5 shows the local reproducing kernels that require modification according to Eq. (5.8) in response to the newly added particle.

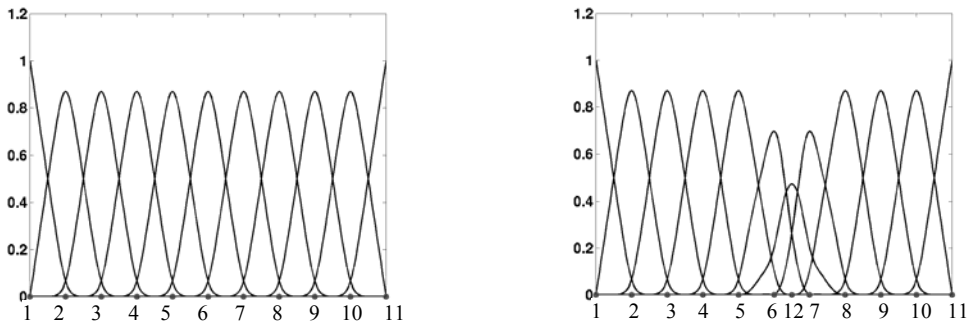


Figure 5.4 Local reconstruction of shape function: (a) before adaptivity (b) after adaptivity

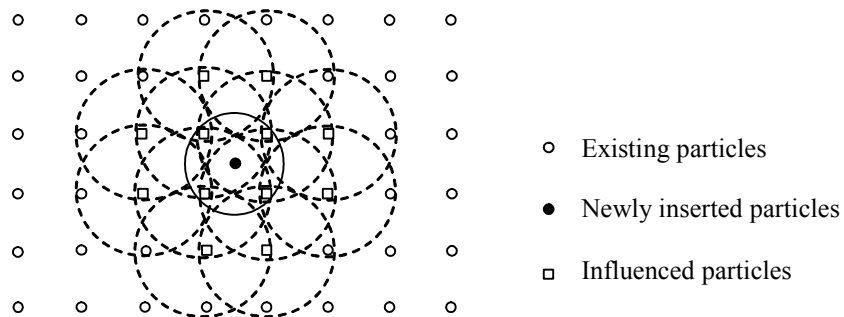


Figure 5.5 Particles influenced by the newly inserted particle in adaptive refinement

In adaptive refinement, the reproducing kernel support sizes need to be properly determined. This can be done by using the Voronoi cell information. Using the Voronoi diagram, we first identify and group the neighboring particles of particle  $I$  as  $B_I$  as shown in Fig. 5.6 below.

$$B_I = \{P_J : V(P_J) \cap V(P_I) \neq \emptyset\}. \quad (5.9)$$

The support size  $a_I$  of particle  $P_I$  is selected as

$$a_I = \alpha_I \cdot \max\{d_J : d_J = \overline{P_I P_J}, \forall P_J \in B_I\}. \quad (5.10)$$

In practice,  $\alpha_I$  is chosen between 1.0 and 2.0 (Lu and Chen, 2002).

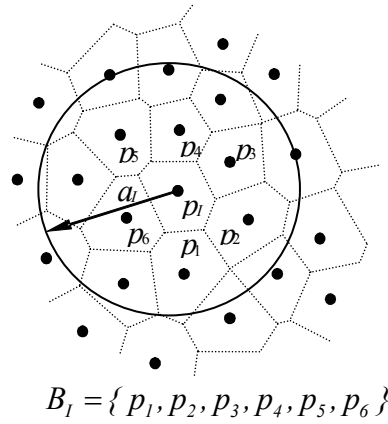


Figure 5.6 Determination of shape function support size

## 6. Numerical Examples

The error indicators described in Sections 4 and 5 are used herein for meshfree adaptive analysis. Reproducing kernel shape functions with linear basis and cubic B-spline kernel function are employed to obtain the meshfree solution. We employ reproducing kernel filter with reproducing order identical to that of the reproducing kernel shape function in meshfree analysis.

### 6.1 Problem with high gradient

We analyze a one-dimensional ordinary differential equation with boundary conditions given below:

$$\begin{aligned}
 u''(x) + g(x) &= 0, \quad \text{on } (-1, 1) \\
 g(x) &= \frac{2 \times 10^6 x}{(1 + 10^4 x^2)^2} \\
 u(-1) &= \arctan(-100) \\
 u(1) &= \arctan(100)
 \end{aligned} \tag{6.1}$$

The exact solution of this example,  $u(x) = \arctan(100x)$ , has a high gradient around point  $x = 0$ . The true error and error indicator of the numerical solution for coarse model with 11 particles and normalized support size  $a = 1.1$  are plotted in Fig. 6.1. Based on the error indicator that correctly locates the region of high gradient, it is possible to construct the adaptive model by inserting two particles at  $x = -0.05$  and  $x = 0.05$ . The true error and error indicator of the

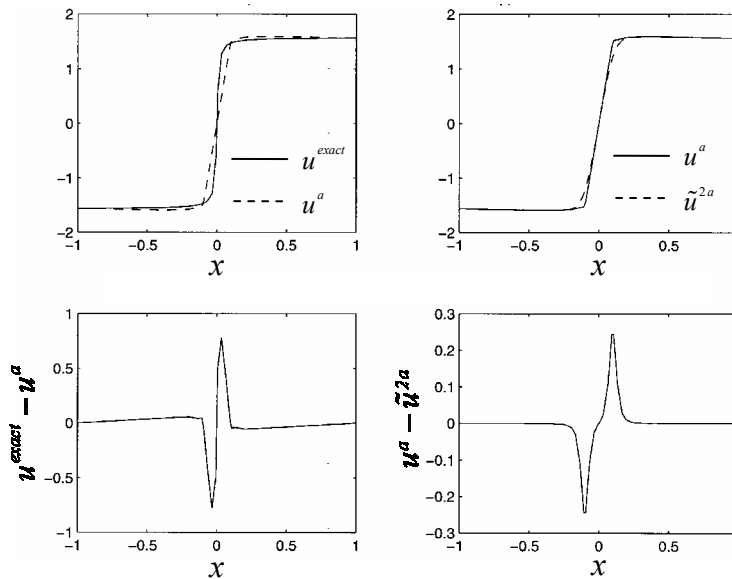
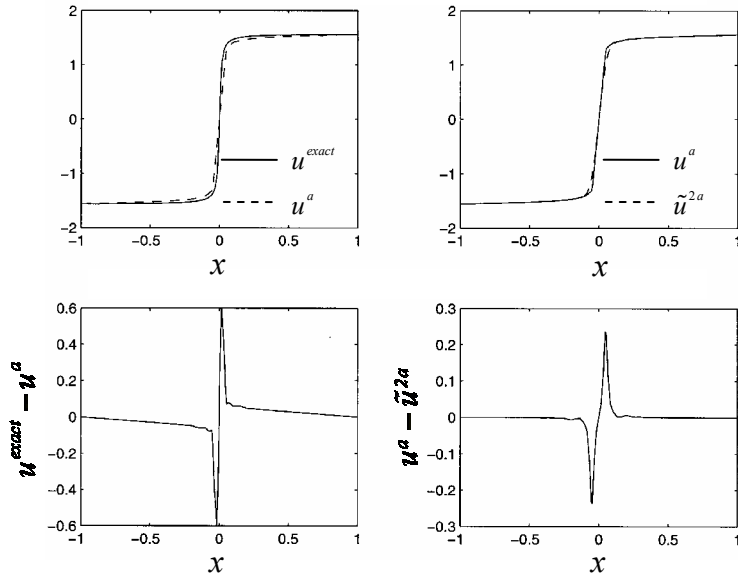
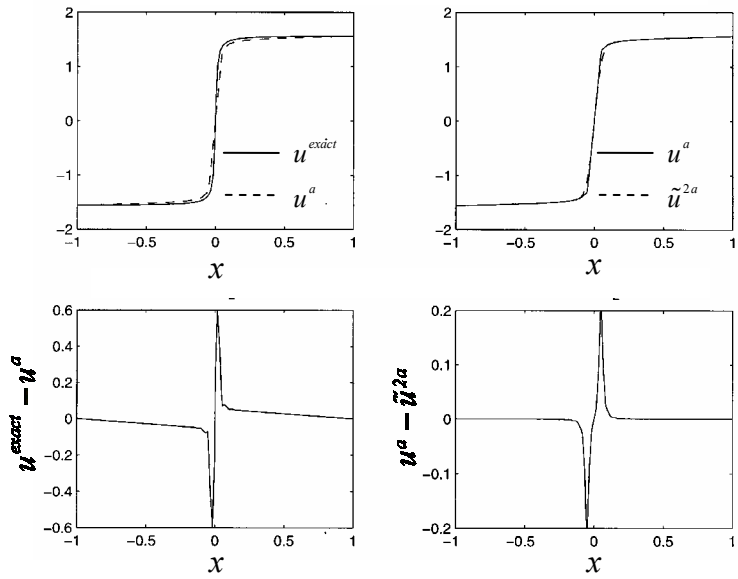


Figure 6.1 The true error and error indicator of the numerical solution for a coarse model



(a) Adaptive model with 13 particles



(b) full refinement model with 41 particles

Figure 6.2 Comparison of the results of: (a) adaptive model (b) full refinement model.

13-particle adaptive model are illustrated in Fig. 6.2 (a) showing improved solution. We use a uniformly refined model with 41 particles for comparison with the adaptive model as shown in Fig. 6.2 (b). The adaptive model with two additional particles provides nearly as much solution accuracy as the uniformly refined model.

## 6.2 Problem with near-singularity

Consider the following problem:

$$\begin{aligned}
 u'' &= g(x) = -\left(\frac{2}{\alpha^2} - \frac{4(x-0.5)^2}{\alpha^4}\right) \exp\left(-\left(\frac{x-0.5}{\alpha}\right)^2\right), \quad \text{on } (0,1) \\
 u(0) &= \exp\left(-\left(\frac{0.5}{\alpha}\right)^2\right) \\
 u'(1) &= -2\left(\frac{1-0.5}{\alpha^2}\right) \exp\left(-\left(\frac{1-0.5}{\alpha}\right)^2\right)
 \end{aligned} \tag{6.2}$$

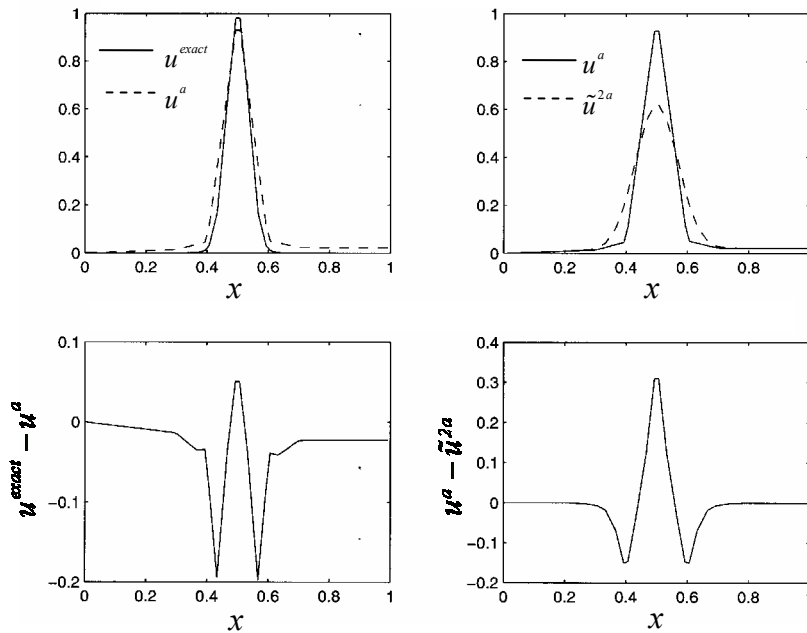


Figure 6.3 The true error and error indicator of the numerical solution for a model with 11 particles

The exact solution of this problem,  $u(x) = \exp(-(\frac{x-0.5}{\alpha})^2)$ , exhibits nearly singular behavior at point  $x = 0.5$  that is characterized by the small value for  $\alpha$ . The numerical solution of the coarse model using 11 particles and normalized support size 1.1 is illustrated in Fig 6.3, and the error indicator shown in the figure has properly detected the location with larger errors.

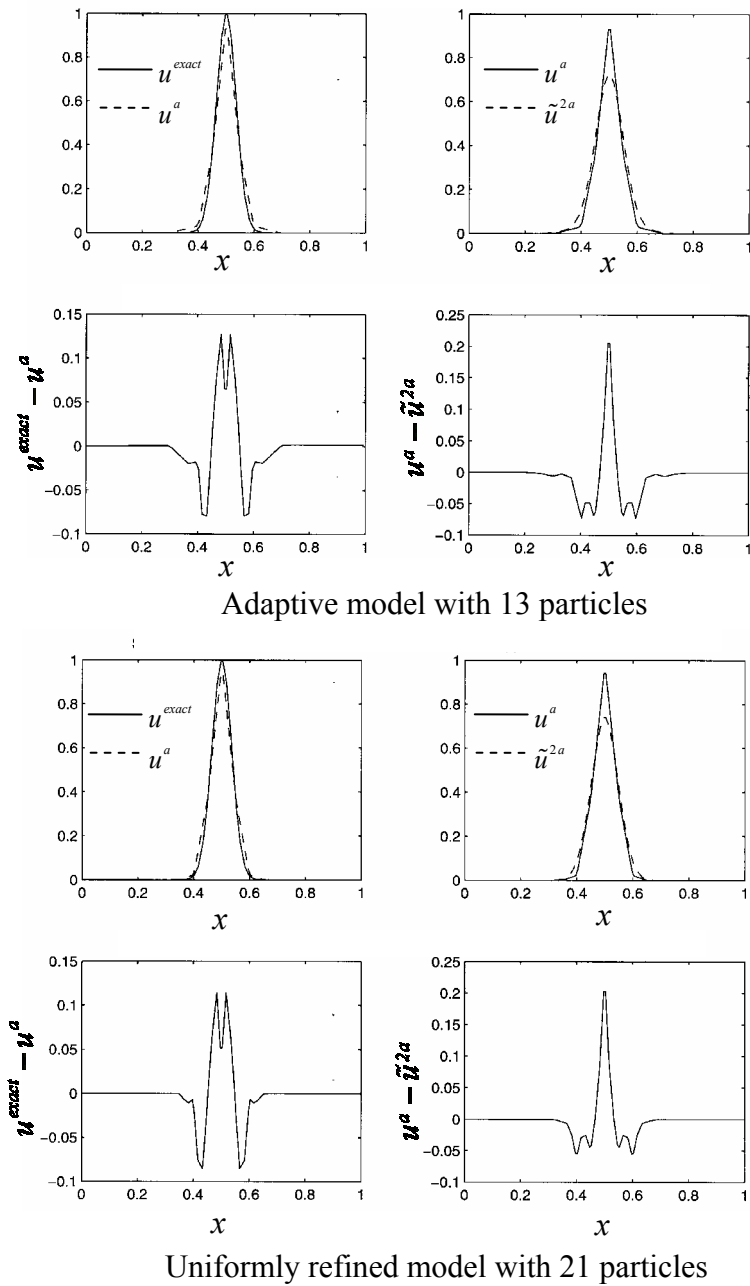
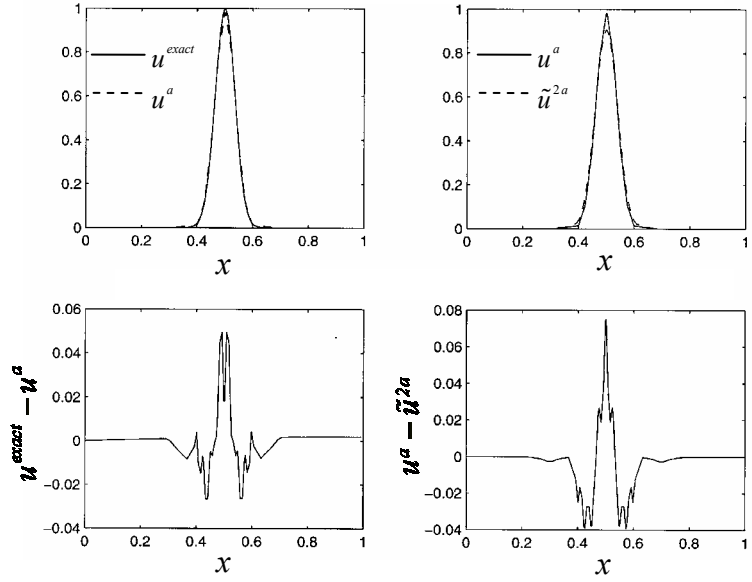
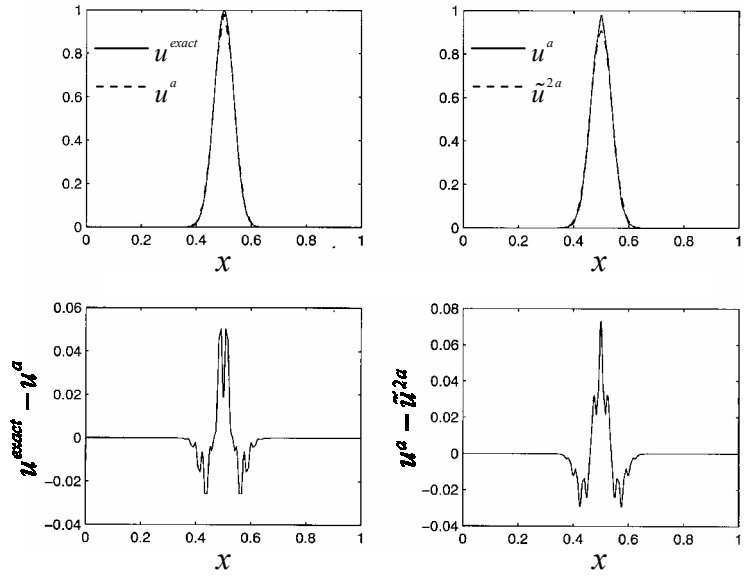


Figure 6.4 (a) First level adaptive and uniform refinements

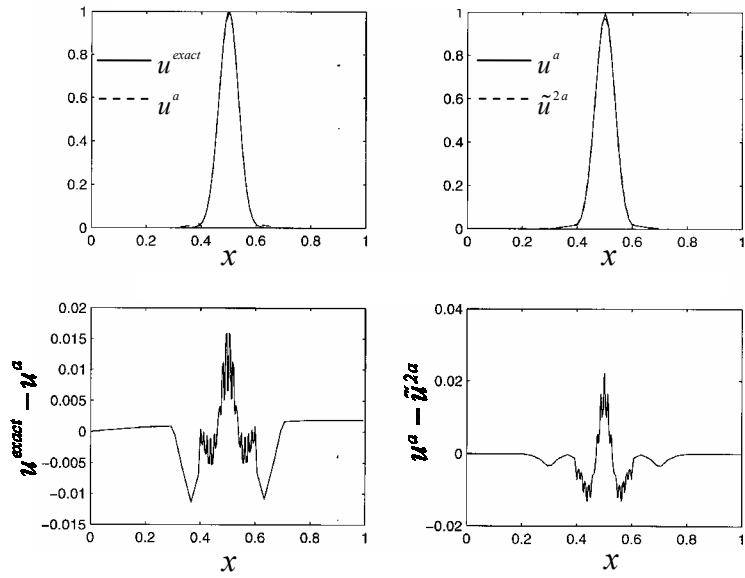


Adaptive model with 17 particles

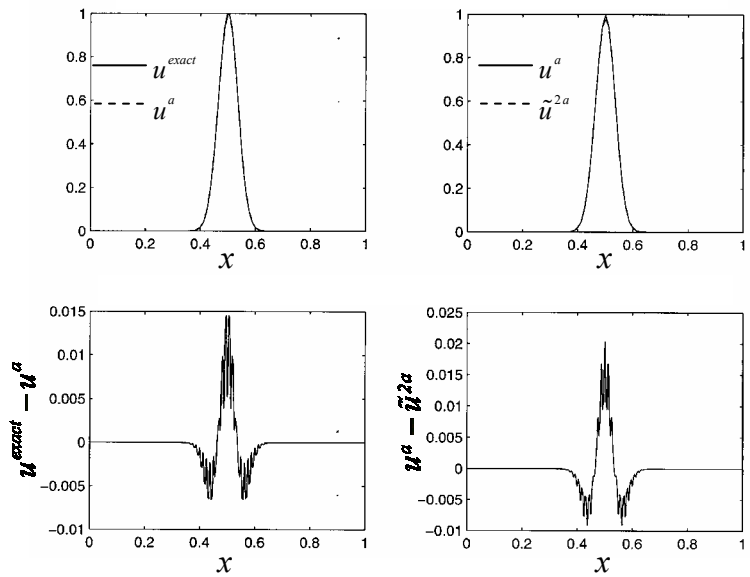


Uniformly refined model with 41 particles

Figure 6.4 (b) Second level adaptive and uniform refinements



Adaptive model with 25 particles



Uniformly refined model with 81 particles

Figure 6.4 (c) Third level adaptive and uniform refinements

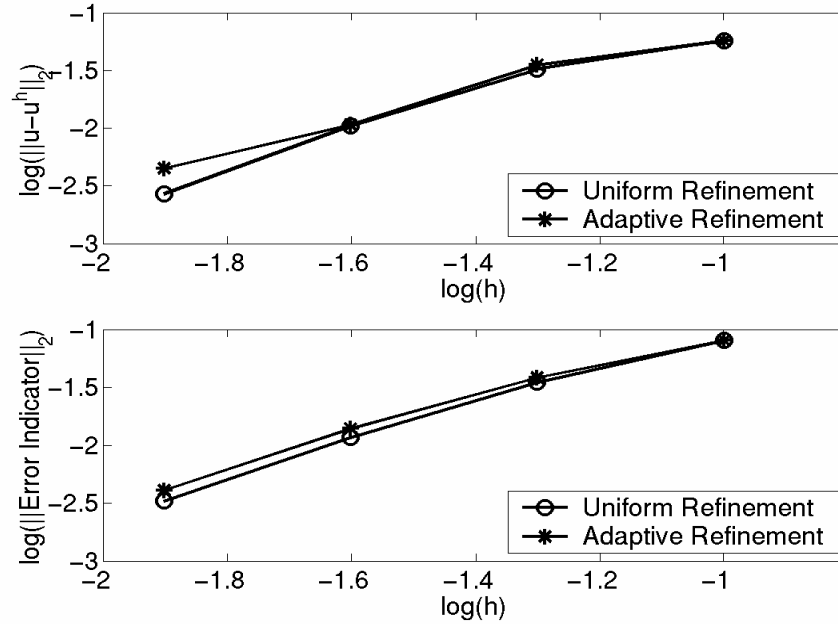


Figure 6.5 The comparison of true error norm and the error indicator norm

Several levels of adaptive models with 13, 17, and 25 particles are generated based on the error indicator. The solution of adaptive models and the corresponding true error and error indicators are shown in Figs. 6.4 (a)-(c). The solutions of uniformly refined models with 21, 41, and 81 particles and the corresponding true errors and error indicators also are plotted in Figs. 6.4 (a)-(c) for comparison. The convergence of the true error norm and the error indicator norm is plotted in Fig. 6.5 for adaptive and uniformly refined models. The results show that the adaptive method reduces the solution error very effectively.

### 6.3 Adaptive Analysis of Plate with a Hole

An infinite plate with a central circular hole is subjected to a unit traction in the x direction as shown in Fig. 6.6. Plane strain conditions were assumed with Young's modulus  $E = 2.11 \times 10^2$  and Poisson's ratio  $\nu = 0.3$ . Due to two-fold symmetry, only the upper right quadrant is modeled in Fig. 6.6. For comparison with the solution of adaptive models, we generate three uniformly refined models as shown in Fig. 6.7. Three levels of adaptive refinements constructed based on the energy error density indicator are shown in Fig. 6.8. The energy error density indicator agrees

with the true energy error density given in Fig. 6.9. The stress distributions obtained by uniformly refined (493 particles) and adaptively refined (153 particles) models are compared in Fig. 6.9 (a). The energy error norms shown in Fig. 6.9 (b) demonstrate how an adaptive method can achieve the same level of accuracy with much fewer particles compared to the uniformly refined method.

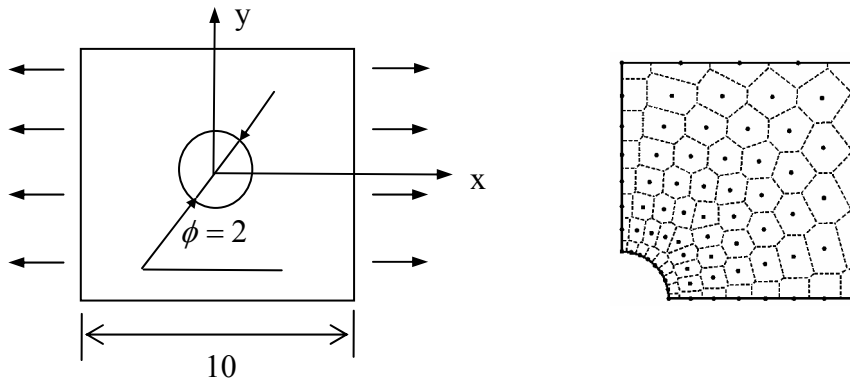
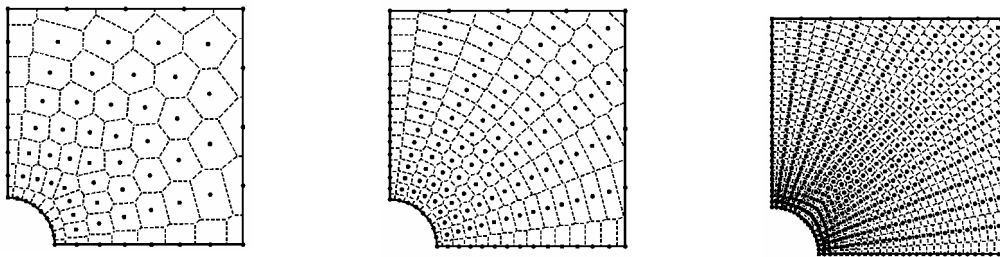


Figure 6.6 Problem description of for plate with a hole



(a) 72 particles

(b) 135 particles

(c) 493 particles

Figure 6.7 Uniformly refined models

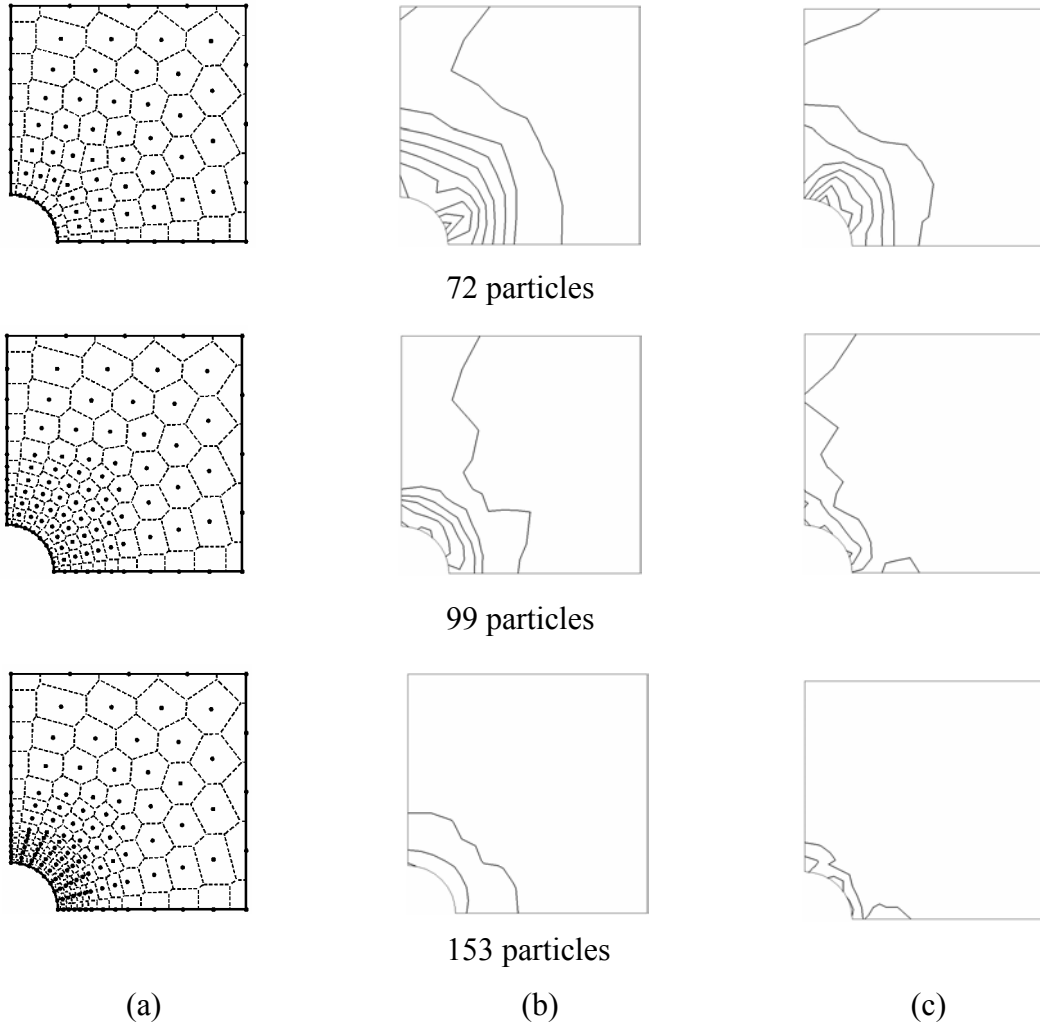
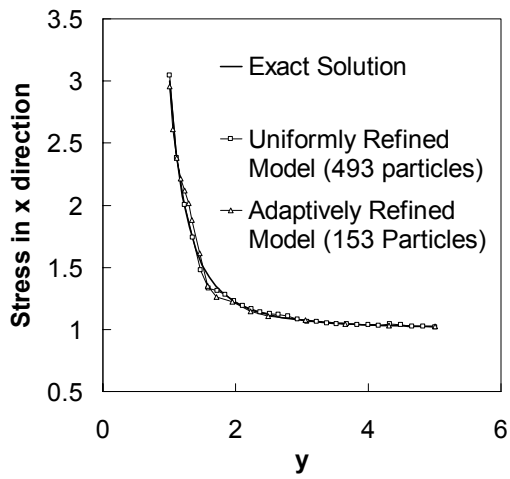
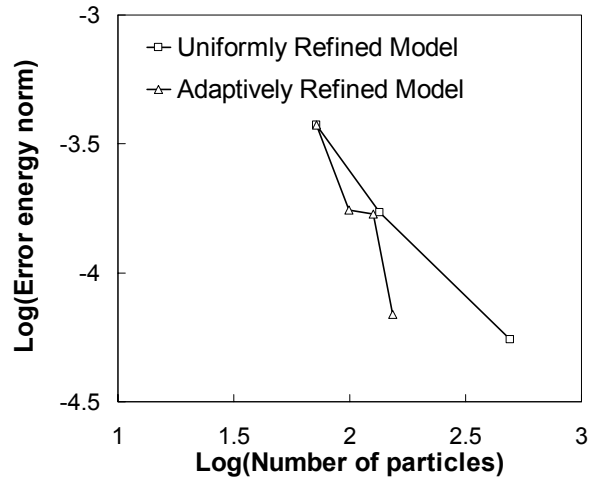


Figure 6.8 (a) Adaptive refinement; (b) Corresponding energy error density indicator; (c) True energy error density indicator.



(a) Stress



(b) Energy error norms

Figure 6.9 Comparison of solutions of uniform and adaptive refinement models

## 7. Conclusion

The reproducing kernel offers several useful properties when used as a filter kernel. The order of the reproducing condition and the support size of the kernel function are the two control parameters in the construction of reproducing kernel as a low-pass filter. We showed that the pass-band expands as the reproducing order of the kernel function increases. On the other hand, increasing the support size while keeping the reproducing order fixed leads to a shrinking pass-band in its spectrum.

The build-in features of the reproducing kernel result in a special low-pass filter where the polynomials of degree less than or equal to the reproducing order are completely retained. We showed that the  $n^{\text{th}}$  order reproducing kernel approximation filtered through an  $m^{\text{th}}$  order reproducing kernel low-pass filter results in a filtered reproducing kernel approximation with reproducing order of  $\min(m,n)$ . Thus by passing the reproducing kernel meshfree solution through the reproducing kernel low-pass filter, only the higher order component of the meshfree solution is partially filtered. Consequently the output of the corresponding high-pass filter captures the higher order portion of the numerical solution. This property is utilized in the reproducing kernel meshfree analysis to form an error indicator.

In conjunction with the reproducing kernel error indicator, an adaptive meshfree method was introduced. The naturally conforming property of the reproducing kernel approximation presents considerable advantages in meshfree adaptive analysis. It allows arbitrary particle insertion and deletion in the adaptive refinement without the burden of the compatibility requirement in the finite element adaptivity procedures. Adaptive refinement based on the Voronoi diagram provides a natural way for particle insertion. Some numerical examples were presented to demonstrate the effectiveness of the proposed error indicator and the adaptive meshfree method.

## ACKNOWLEDGEMENT

The Support of this work by the NSF/DARPA OPAAL Program under the grant DMS 98-74015 to UCLA is greatly acknowledged.

## Reference

1. Aurenhammer, F. (1991), "Voronoi Diagram: A Survey of a Fundamental Geometric Data Structure," *ACM Comp. Surveys*, 23, 345-405.
2. Blinchikoff, H. J., and Zverev, A. I. (1976), "Filtering in the Time and Frequency Domains," John Wiley.
3. Chui, C. K. (1992), "An Introduction to Wavelets," Academic, New York.
4. Chen, J. S., Pan, C., Wu, C. T., and Liu, W. K. (1996), "Reproducing Kernel Particle Methods for Large Deformation Analysis of Nonlinear Structures," *Computer Methods in Applied Mechanics and Engineering*, 139, 195-227.
5. Chen, J. S. and Wang, H. P. (2000), "New Boundary Condition Treatments for Meshless Computation of Contact Problems," *Comput. Meth. Appl. Mech. Engng.*, 187, 441-468.
6. Chen, J. S., Wu, C. T., Yoon, S., and You, Y. (2001), "A Stabilized Conforming Nodal Integration for Galerkin Mesh-free Methods," *Int. J. Numer. Meth. Eng.*, 50, 435-466.
7. Daubechies, (1992), "Ten Lectures on Wavelets," *CBMS/NSF Series in Applied Mathematics*, No 61.
8. Kalouptsidis, N. (1996), "Signal Processing Systems: Theory and Design," John Wiley and Sons.
9. Li, S. and Liu, W. K. (1996), "Moving Least Square Reproducing Kernel Method, Part II: Fourier Analysis," *Computer Methods in Applied Mechanics and Engineering*, 139, 159-194.
10. Li, S. and Liu, W. K. (1999), "Reproducing Kernel Hierarchical Partition of Unity, Part I: Formulation and Theory", *International Journal for Numerical Methods in Engineering*, 45, 251-288.
11. Liu, W. K. (1995a), "An Introduction to Wavelet Reproducing Kernel Particle Methods," *USACM bulletin*.

12. Liu, W. K. and Chen, Y. J. (1995b), "Wavlet and Multiple Scale Reproducing Kernel Particle Methods," *International Journal for Numerical Methods in Fluids*, 21, 901-932.
13. Liu, W. K., Jun, S., Li, S., Adee, J., and Belytschko, T. (1995c), "Reproducing Kernel Particle Methods for Structural Dynamics," *Int. J. Numer. Meth. Eng.*, 38, 1655-1679.
14. Liu, W. K., Chen, Y., Chang, C. T., and Belytschko, T. (1996), "Advances in Multiple Scale Kernel Particle Methods," *Computational Mechanics*, 18, 73-111.
15. Liu, W. K., Jun, S., Sihling, D. T., Chen, Y., and Hao, W. (1997a), "Multiresolution Reproducing Kernel Particle Method for Computational Fluid Dynamics," *International Journal of Numerical Methods in Fluids*, 24, 1391-1415.
16. Liu, W. K., Hao, W., Chen, Y., et al. (1997b), "Multiresolution Reproducing Kernel Particle Methods," *Computational Mechanics*, 20, 295-309.
17. Liu, G.R. and Tu, Z. H. (2002), "An adaptive procedure based on background cells for meshless methods," *Computer Methods in applied Mechanics and Engineering* 191, 1923-1943.
18. Lu, H., and Chen, J. S. (2002), "Adaptive Galerkin Particle Method", *Lecture Notes in Computational Science and Engineering*, 26, 251-267.
19. Sheno, K. (1995), "Digital Signal Processing in Telecommunications," Prentice Hall.
20. Smith, S. W. (1997), "The Scientist and Engineer's Guide to Digital Signal Processing", California Technical Publishing.
21. Strang, G. and Nguyen, T. (1996), "Wavelets and Filter Banks", Wellesley-Cambridge Press.